Nonstoichiometry in the Zintl Phase $Yb_{1-\delta}Zn_2Sb_2$ as a Route to Thermoelectric Optimization

Alex Zevalkink,[†,‡] Wolfgang G. Zeier,[†] Ethan Cheng,[‡] Jeffrey Snyder,*[†] Jean-Pierre Fleurial,[‡] and Sabah Bux*[‡]

[†]Material Science, California Institute of Technology, Pasadena, California 91125, United States

[‡]Jet Propulsion Laboratory, 4800 Oak Grove Drive, Pasadena, California 91109, United States

Ⓢ *Supporting Information*

ABSTRACT: Classically, Zintl phases are defined as valence-precise line compounds and are thus expected to exhibit intrinsic semiconducting behavior. Contradicting this definition are AZn_2Sb_2 Zintl compounds (A = Ca, Sr, Eu, Yb), which exhibit metallic behavior due to high concentrations of cation vacancies, according to recent density functional calculations. Here, we use synchrotron diffraction and high-temperature electronic and thermal transport properties to show that the phase width of $Yb_{1-\delta}Zn_2Sb_2$ is wide enough to allow for significant variation and optimization of the thermoelectric properties within the single phase region. Samples with nominal compositions of $Yb_xZn_2Sb_2$ ($0.98 < x < 1.05$) were synthesized using a solid-state process. With decreasing synthetic Yb content, synchrotron X-ray diffraction reveals decreased lattice parameters, decreased occupancy of the Yb site, and a relaxation of the tetrahedral angles within the Zn_2Sb_2 sheets. In Yb-deficient samples, the carrier concentration can

be controlled by varying x, whereas, in samples with excess Yb, the carrier concentration remains constant and p-type. Fully intrinsic semiconducting behavior was not obtained, suggesting that a slightly Yb-deficient composition is thermodynamically preferable to the valence-precise stoichiometry of $\delta = 0$. Tuning the vacancy concentration provides a new route to controlling the electronic properties in $Yb_{1-\delta}Zn_2Sb_2$ and leads to a 50% improvement in the thermoelectric figure of merit ($zT = 0.85$ at 773 K) compared to previously reported values for unalloyed $YbZn_2Sb_2$.
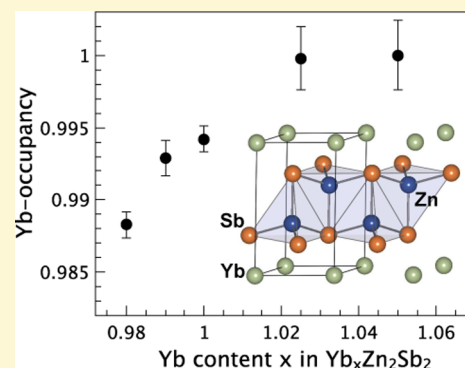
INTRODUCTION

The maximum thermal-to-electrical conversion efficiency of thermoelectric materials depends on the thermoelectric figure of merit, given by $zT = ((\sigma \alpha^2 T)/\kappa)$. An ideal thermoelectric material must strike a balance between the conflicting requirements of a high Seebeck coefficient, α, high electronic conductivity, σ, and low thermal conductivity, κ.[1] Zintl phases, a subset of intermetallic compounds characterized by covalently bonded polyanions, surrounded by highly electropositive cations, exhibit many of the characteristics desired for thermoelectric applications.[2–4] The requirement that Zintl compounds satisfy the valence of anions through the formation of covalent substructures leads to many unique, complex crystal structures, and thus to low lattice thermal conductivity.[5] Excellent thermoelectric performance ($zT \sim 1$) has been demonstrated in several Zintl phases.[6–8] Additionally, many Zintl phases, though not yet optimized for thermoelectric applications, are promising candidates.[9–15]

AM_2Sb_2 phases where A = Sr, Ca, Yb, Eu and M = Zn, Mn, Cd are of particular interest for thermoelectric applications. These comounds form in the $CaAl_2Si_2$ structure type, which is characterized by two-dimensional $(M_2Sb_2)^{2-}$ slabs sandwiched between layers of A^{2+} cations. The structure has been described in detail by Burdett and Miller using the Zintl formalism.[17] AM_2Sb_2 compounds benefit from very high electronic mobility,

leading to peak zT values as high as 1.2 at 773 K in optimally alloyed samples.[6,18–27]

As nominally valence-precise compounds, AM_2Sb_2 phases should behave as intrinsic semiconductors with low carrier concentrations ($\sim 10^{18}$ cm^{-3}) at room temperature.[4,7,28,29] Contrary to expectations, these phases often exhibit high experimental carrier concentrations (10^{19}–10^{20} cm^{-3}) and extrinsic semiconducting behavior.[6,18–22,25,26] Similar behavior was also reported in AMg_2Bi_2 compounds with the same structure type.[30,31] We recently demonstrated using density functional theory that this remarkable behavior can be explained by large concentrations of thermodynamically stable cation vacancies.[16] It is well-known that vacancies can control the electronic properties of a diverse range of thermoelectric materials, including oxides,[32] clathrates,[33] and the rock salt chalcogenides.[34] In Zintl phases, however, the effect of vacancies had not been widely investigated.[16,35]

To confirm our previously reported computational results, we present herein an experimental investigation of $Yb_{1-\delta}Zn_2Sb_2$. The Yb analogue was chosen because it has the largest predicted vacancy concentration among AZn_2Sb_2

phases. Shown in Figure 1, the calculated $ZnSb-YbZn_2Sb_2$ phase diagram illustrates the Yb-deficient stability limit (solid
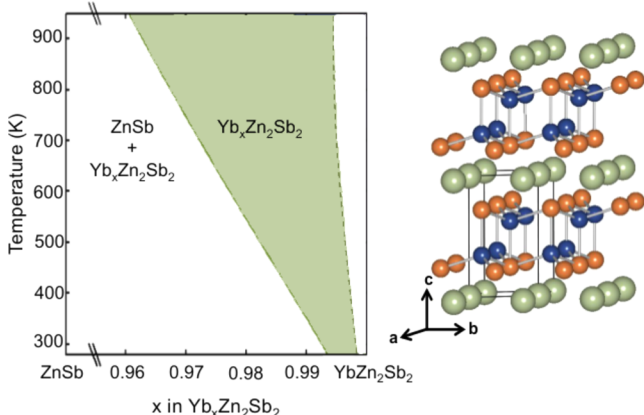

Figure 1. Left: The calculated $ZnSb-YbZn_2Sb_2$ phase diagram[16] illustrates the large stable concentration of cation vacancies tolerated by $Yb_xZn_2Sb_2$. The dashed boundary is the proposed upper limit to the Yb content. Right: The $YbZn_2Sb_2$ structure is characterized by covalent $(Zn_2Sb_2)^{2-}$ slabs between layers of Yb^{2+} cations. Yb is shown in green, Zn in blue, and Sb in orange.

curve) for $Yb_{1-\delta}Zn_2Sb_2$ as a function of temperature. At 800 K, a Yb content as low as $Yb_{0.967}Zn_2Sb_2$ is stable, corresponding to a Yb vacancy concentration of 2.2×10^{20} cm^{-3} and a predicted charge carrier concentration of 1.6×10^{20} $holes/cm^3$.[16] This suggests that nonstoichiometry is responsible for the large experimental carrier concentrations found in $YbZn_2Sb_2$, providing a potential route to controlling the electronic properties by varying the Yb content. In the present study, Yb-deficient and Yb-rich samples were synthesized with nominal compositions of $Yb_xZn_2Sb_2$ (x = 0.98, 0.99, 1.00, 1.025, 1.05), and their high-temperature electronic and thermal transport properties and synchrotron X-ray diffraction patterns are presented. The results are used to optimize and improve the thermoelectric performance of $Yb_{1-\delta}Zn_2Sb_2$ and to refine our understanding of the defect chemistry in AZn_2Sb_2 phases as well as other compounds with the $CaAl_2Si_2$ structure type.

■ EXPERIMENTAL SECTION

Synthesis. Bulk samples with nominal compositions of $Yb_xZn_2Sb_2$ (x = 0.98, 0.99, 1.00, 1.025, and 1.05) were prepared via ball-milling, followed by hot pressing, starting with elemental precursors. The elements (99.99% Yb ingot, 99.99% Zn ingot, and 99.999% Sb shot from Alpha Aesar) were cut into small pieces and loaded into 65 mL stainless-steel vials with three 12.7 mm stainless-steel balls in an Ar drybox. The contents were dry ball-milled for 2 h using a SPEX Sample Prep 8000 Series Mixer/Mill. The resulting fine powder was consolidated in a hot press in high-density graphite dies (POCO) in argon for 1.5 h at 823 K using 160 MPa of pressure, and cooled to ambient temperature under argon after the load was removed.

Characterization. The hot pressed samples were sliced into 1 mm thick, 12 mm diameter disks. Phase purity of the samples was monitored on polished slices using standard laboratory X-ray diffraction patterns, collected on a Philips XPERT MPD diffractometer. High-resolution synchrotron powder diffraction data were collected using beamline 11-BM at the Advanced Photon Source (APS), Argonne National Laboratory, using an average wavelength of 0.413708 Å. Because of the high X-ray absorption coefficient of the compositions, the powder was diluted with amorphous SiO_2 prior to the measurements at the synchrotron. The resulting diffraction data were refined using the General Structure Analysis System (GSAS).[36]

An experimental uncertainty of the lattice parameters of 0.0001 Å has been determined through a refinement of the 11-BM $Na_2Ca_3Al_2F_{14}$ standard. Longitudinal and transverse ultrasonic measurements were performed at room temperature to obtain the longitudinal and transverse sound velocities. High-temperature electronic properties were characterized up to 973 K under dynamic vacuum. The Seebeck coefficients were measured using the light-pipe method with tungsten–niobium thermocouples under high vacuum in a custom setup.[37] Temperature-dependent Hall coefficients and resistivity (Van der Pauw 4-point probe) were measured using a 0.8 T magnet with tungsten pressure contact probes.[38] A Netzsch LFA 457 was used to measure the thermal diffusivity to 973 K. The combined measurement uncertainty in the thermoelectric figure of merit is generally assumed to be approximately 20%.

■ RESULTS AND DISCUSSION

Structural Characterization. The hot pressed, polycrystalline $Yb_xZn_2Sb_2$ samples were dense (from 96% to 99% of theoretical) and stable in air. Standard laboratory X-ray diffraction was employed to confirm phase purity. The samples with compositions x = 0.98–1.025 were found to be phase pure. However, the sample with x = 1.05 exhibits extra reflections, consistent with the presence of $Yb_9Zn_{4.5}Sb_9$,[39] which was also observed using energy-dispersive spectroscopy and scanning electron microscopy. These results are roughly consistent with the $ZnSb-YbZn_2Sb_2$ phase diagram (Figure 1), which suggests that Yb-deficient samples should be phase pure. The predicted phase diagram does not tell us what to expect on the Yb-rich side. Most likely, Yb-rich samples (as well as the sample with x = 1.00, potentially) are in either a two or a three phase region formed by $YbZn_2Sb_2$, $Yb_9Zn_{4.5}Sb_9$, and possibly a Sb-deficient binary phase.

To obtain a better resolution of the lattice parameters and atomic positions, synchrotron radiation was used. Figure 2
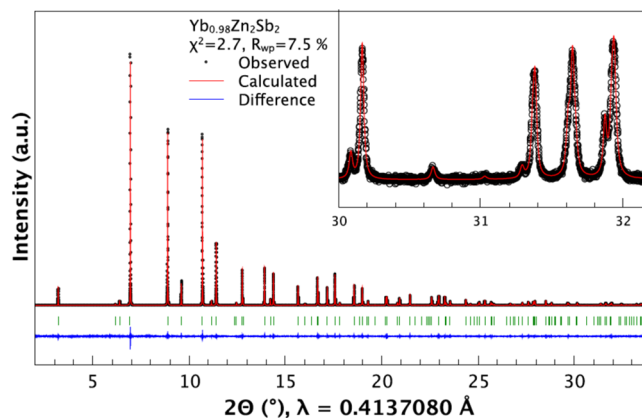

Figure 2. Representative synchrotron diffraction data of the sample with nominal composition $Yb_{0.98}Zn_2Sb_2$, including profile fit, profile difference. and profile residuals (χ^2 and R_{wp}) of the corresponding Rietveld refinement. The inset shows the goodness of fit at high angles.

shows the diffraction pattern of $Yb_{0.98}Zn_2Sb_2$, representative for all samples. The space group $P\bar{3}m1$ and the structural data of $YbZn_2Sb_2$[40] were used as the initial structural model, and the input for the various solid solutions was altered accordingly. Refinements of the Yb occupancies were conducted with a constant U_{iso} along the series of solid solutions for comparison. A fixed value of 100% for the sample with the nominal composition of $Yb_{1.05}Zn_2Sb_2$ has been used to show the trend in the occupancy of the changing Yb content. The resulting unit

5711

dx.doi.org/10.1021/cm502588r | Chem. Mater. 2014, 26, 5710–5717

Table 1. Refined Unit Cell Parameters a, c, V, and Atomic Positions for Zn and Sb from the Rietveld Refinement of the Solid Solutions of $Yb_xZn_2Sb_2$ (Space Group $P\bar{3}m1$) against Synchrotron X-ray Powder Diffraction Data from 11-BM with the Respective Reduced χ^2 (Goodness of Fit) and R_{wp} (Weighted Profile Residual)^a

	$x = 0.98$	$x = 0.99$	$x = 1.00$	$x = 1.025$	$x = 1.05$
χ^2	2.7	3.7	1.8	1.6	4.7
R_{wp} (%)	7.5	9.6	7.4	11.5	13.1
a (Å)	4.441794(3)	4.442424(4)	4.442524(4)	4.442828(11)	4.443363(13)
c (Å)	7.425132(9)	7.426813(12)	7.429091(12)	7.43049(4)	7.43150(4)
V (Å^2)	126.8680(2)	126.9330(3)	126.9770(3)	127.0180(10)	127.0660(10)
Yb (x,y,z)	(0,0,0)	(0,0,0)	(0,0,0)	(0,0,0)	(0,0,0)
Zn (x,y,z)	($^1/_3$,$^2/_3$,0.63198(6))	($^1/_3$,$^2/_3$,0.63184(8))	($^1/_3$,$^2/_3$,0.63183(6))	($^1/_3$,$^2/_3$,0.63217(14))	($^1/_3$,$^2/_3$,0.63214(13))
Sb (x,y,z)	($^1/_3$,$^2/_3$,0.25701(4))	($^1/_3$,$^2/_3$,0.25723(6))	($^1/_3$,$^2/_3$,0.25727(4))	($^1/_3$,$^2/_3$,0.25736(10))	($^1/_3$,$^2/_3$,0.25732(9))

^{a}Diffraction data were obtained at room temperature.

cell parameters, refined atomic positions, and profile residuals can be found in Table 1.

The refined unit cell parameters a, c, and V against the nominal Yb content, x, are shown in Figure 3. While the
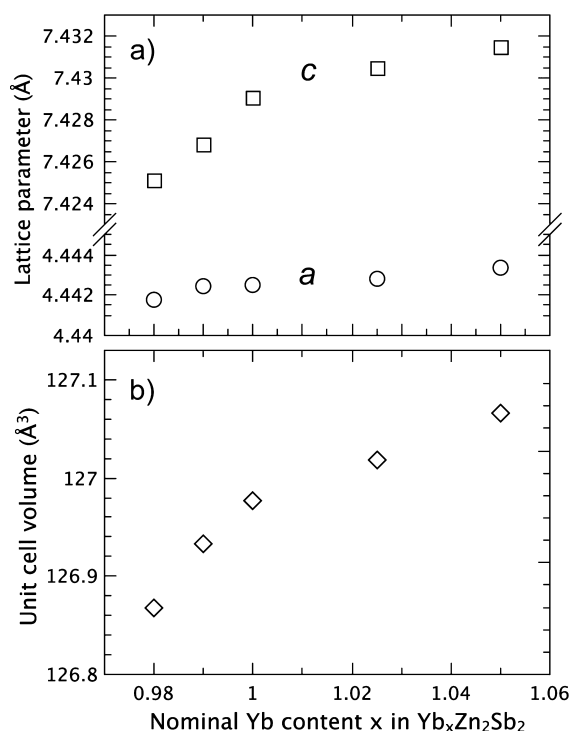

Figure 3. (a) Refined lattice parameters a and c and (b) the unit cell volume, V, of $Yb_xZn_2Sb_2$ samples exhibit a linear trend when $x < 1.00$, associated with Vegard-like behavior. As expected, a lower Yb content leads to smaller lattice parameters. The change of slope shows that a solubility limit has been reached for $x > 1.00$. Because of the nature of the sheetlike structure, the effect is more pronounced for the lattice parameter in the z direction (c axis).

compositions with x greater than unity indicate that a solubility limit has been reached, the Yb-deficient samples show a linear Vegard-like behavior of the lattice. A decreasing Yb content leads to a decrease in the lattice parameters. This trend is more pronounced along the z direction (c axis), perpendicular to the Zn_2Sb_2 sheets, consistent with the formation of Yb vacancies (see Figures 1 and 4). Figure 4 shows the refined Yb occupancy as a function of the nominal Yb content, x. As expected, the refined occupancies decrease when the Yb content is below $x = 1$, confirming that these samples are nonstoichiometric.
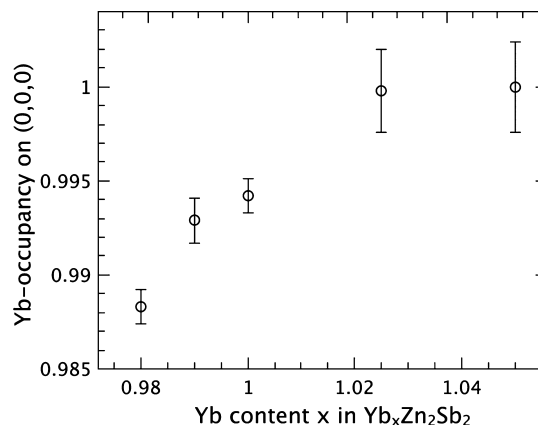

Figure 4. Refined Yb occupancy in $Yb_xZn_2Sb_2$ on Wyckoff position 1a (0,0,0) decreases with decreasing nominal Yb content, x.

However, the magnitude of the reduction obtained from refinements is somewhat less than the anticipated linear dependence on x.

As mentioned above, the structure consists of two-dimensional $(Zn_2Sb_2)^{2-}$ slabs with $ZnSb_4$ tetrahedral and $SbZn_4$ inverted-tetrahedral motifs.[17] In order to understand the influence of the Yb deficiency on this structural motif, the average bond angles for the $ZnSb_4$ tetrahedra, obtained from the refined atomic positions, are shown in Figure 5. There are two distinct angles in the tetrahedra (see schematic in Figure 5), namely, the basal angle (Sb−Zn−Sb 1) and the angle between the base and the z direction (Sb−Zn−Sb 2). The decreasing volume of the lattice with decreasing Yb content leads to a change of both angles, approaching the ideal tetrahedral angle of 109.5° for the more Yb-deficient samples. This tendency to achieve the more energetically favored relaxed angle might explain the tendency to form vacancies in this class of materials. It is worth noting, however, that, in the isostructural compound $SrZn_2Sb_2$, the larger Sr cations lead to an even greater degree of distortion of the ideal tetrahedral angles (106.56° and 112.22°), and yet this compound exhibits low carrier concentration and presumably low vacancy concentrations.[25,41] The relaxation of the distorted tetrahedra toward the ideal geometry is, therefore, not a large enough driving force, on its own, to cause vacancy formation in the case of a highly electropositive cation.[16]

Electronic Transport. As a nominally valence-precise Zintl phase, stoichiometric $YbZn_2Sb_2$ is expected to have a very low carrier concentration and intrinsic semiconducting behavior. The presence of Yb vacancies, however, leads to extrinsic p-type
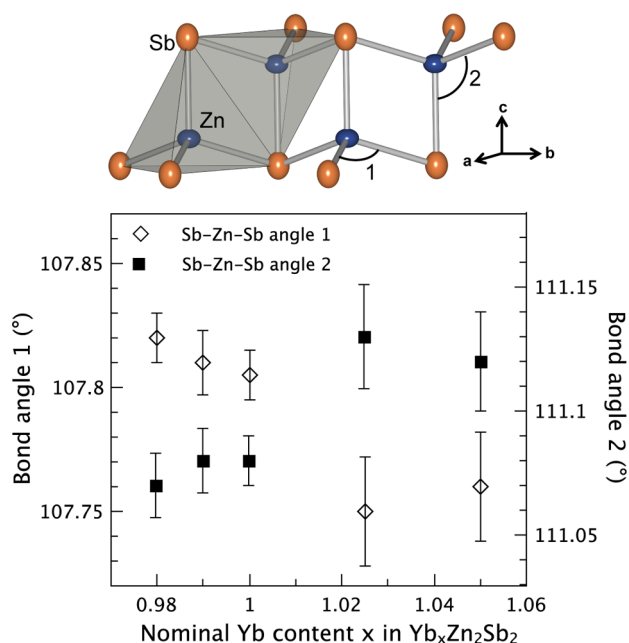
Figure 5. Above: The structure of the $(ZnSb)_2$ sheets showing the refined anisotropic thermal ellipsoids that indicate a predominant thermal motion of Sb in the z direction at room temperature. These parameters increase slightly with increasing Yb content and cell volume. Below: The average bond angles (see diagram above) for the $ZnSb_4$ tetrahedral units, obtained from the refined atomic positions of Zn and Sb. Decreasing Yb content leads to a relaxation of the tetrahedral angles toward the ideal tetrahedral angle of 109.5°.

behavior. At 800 K—close to the temperature at which the samples in this study were consolidated—the calculated maximum Yb vacancy concentration is 2.2×10^{20} cm^{-3}, corresponding to a hole concentration of 1.6×10^{20} cm^{-3}. Note that the charge associated with each Yb vacancy is not always 2+. In fact, at the temperatures of interest, DFT calculations predict that each Yb vacancy contributes closer to 1 free hole.[16,42]

The dotted line in Figure 6 shows the expected dependence of the carrier concentration, n, on the nominal Yb content, x, assuming (a) that the composition of the samples becomes kinetically "frozen" below 800 K, (b) that the vacancy and carrier concentration vary linearly with x within the single phase
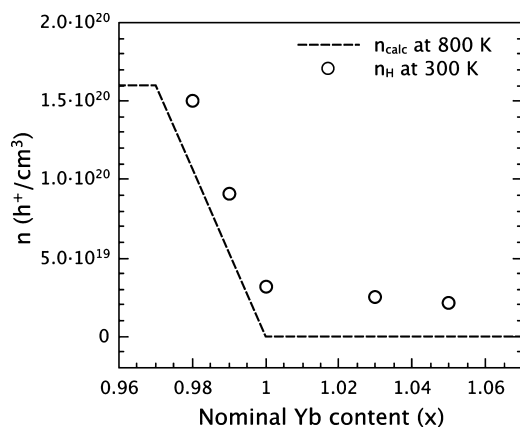

Figure 6. Hall carrier concentration, n_H, of $Yb_xZn_2Sb_2$ samples exhibits roughly the predicted dependence on x, decreasing linearly for $x <$ 1.00 and remaining constant when $x > 1.00$.

region, and (c) that n remains constant outside of the single phase region (i.e., when $x > 1.00$ and $x < 0.967$). Note that one might alternatively predict n-type behavior if the structure tolerates excess Yb in interstitial sites. However, our previous DFT results indicate that this is highly unlikely.[16]

Given these assumptions, the experimental Hall carrier concentrations, n_H, of $Yb_xZn_2Sb_2$ samples agree remarkably well with the predicted values, showing the expected linear dependence on x in the single phase region, and remaining constant when $x > 1.00$. Note, however, that this is not perfectly consistent with the refined Yb-occupancies, which increase between $x = 1.00$ and $x = 1.025$. In samples with excess Yb, the carrier concentration remains relatively high and p-type. This can be understood as follows: Any attempt to increase the Yb content will shift the Fermi level, E_F, upward. As E_F increases, the energy required to form Yb vacancies decreases, thus *increasing* the number of Yb vacancies and effectively pinning E_F in the valence band.[16] These results suggest that a Yb-deficient composition ($\delta > 0$) is thermodynamically preferable to the valence-precise stoichiometry, implying that the phase width of $Yb_{1-\delta}Zn_2Sb_2$ may not fully extend to $\delta = 0$. Using the minimum experimental carrier concentration, we can estimate an upper stability limit for the Yb concentration of approximately $x = 0.995$, which is drawn as a dashed curve in Figure 1.

On the basis of the calculated phase diagram, one might expect ZnSb to precipitate out of the most Yb-deficient sample ($x = 0.98$) below 500 K during repeated thermal cycling, leading to temperature-dependent carrier concentrations in that temperature range. However, the carrier concentration in the Yb-deficient samples remains constant as a function of temperature up to 600 K, which is characteristic of extrinsically doped semiconducting behavior (Figure 7a). This suggests that diffusion in $Yb_xZn_2Sb_2$ may be too slow to allow for the formation of ZnSb during cooling over the course of several hours.

Thermally activated minority carriers lead to increasing n_H beginning at 500 K in samples with $x = 1.00-1.05$, and beginning at 600 K when $x = 0.99$ and $x = 0.98$, respectively. Similar trends are apparent in the resistivity and Seebeck coefficients (Figure 7b,d), both of which increase in magnitude and transition from extrinsic to increasingly intrinsic semiconducting behavior as x increases. The magnitude of the band gap, E_g, can be estimated from the temperature and magnitude at which the Seebeck coefficient peaks ($E_g = 2\alpha_{max}T_{max}$), yielding $E_g = 0.25$ eV, consistent with recent calculations by Flage-Larsen et al.[27]

Figure 8 illustrates the dependence of the Seebeck coefficient on n_H at 300 and 500 K. The calculated band structure of $YbZn_2Sb_2$ contains three bands at the valence band edge that are degenerate at Γ. These can be modeled as a single parabolic band with a single combined effective mass.[25] A rigid band model is likely a valid assumption in this system, as several studies of compounds with the $CaAl_2Si_2$ structure type have indicated that the covalently bonded slabs determine the states near the band gap, while the cation species, size, and the separation distance between the slabs have little influence.[43,44] The dashed curves in Figure 8 correspond to masses of $m^* = 0.6\ m_e$ at 300 K and $m^* = 0.9\ m_e$ at 500 K and assume that acoustic phonons are the primary scattering source. This approximation describes the experimental relationship between α and n reasonably well within the extrinsic temperature regime.
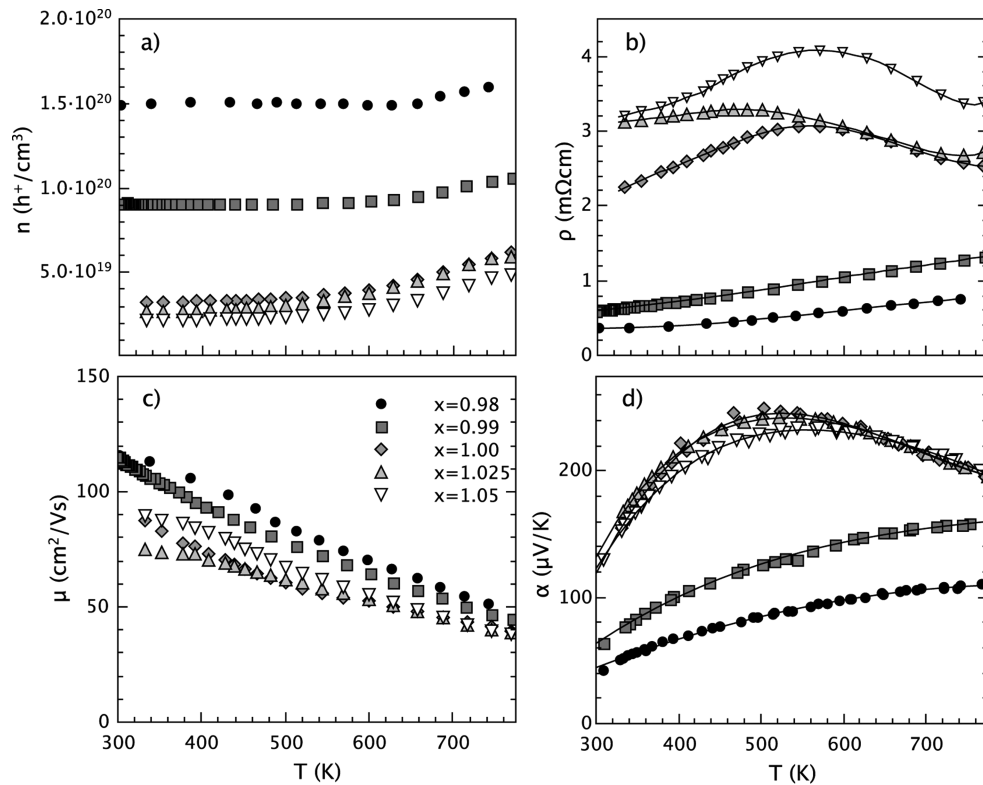
Figure 7. (a) The Hall carrier concentration, (b) resistivity, (c) Hall mobility, (d) and Seebeck coefficients of $Yb_xZn_2Sb_2$ are consistent with a decreasing concentration of Yb vacancies as x increases from 0.98 to 1.00. Above $x = 1.00$, n_H and α remain constant.
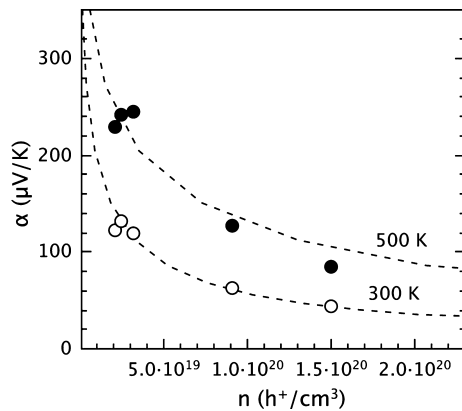

Figure 8. Seebeck coefficients of $Yb_xZn_2Sb_2$ samples decrease with increasing n_H in accordance with a single band model with $m^* = 0.6\ m_e$ at 300 K and $m^* = 0.9\ m_e$ at 500 K.

The Hall mobility (μ_H) at high temperature (Figure 7c) exhibits the $T^{-\nu}$ temperature dependence expected for acoustic phonon scattering, where ν is approximately 1.2.[45] Near room temperature, however, an additional scattering mechanism may be be responsible for a slight suppression in μ, particularly in samples with excess Yb content. The magnitude of μ_H varies significantly (from 75 to 118 cm^2/(V s)) between samples and does not show the expected decrease with increasing n_H. The Hall mobilities measured in the current study are somewhat lower than those in literature reports. Previously reported values for the mobility in $YbZn_2Sb_2$ range from 119 to 130 cm^2/(V s) for polycrystalline samples,[18,19] to 165 cm^2/(V s) for single crystal samples measured along the $a-b$ plane.[26]

Thermal Transport. The total thermal conductivity, κ, and lattice thermal conductivity, κ_L, are shown in Figure 9a,b as a

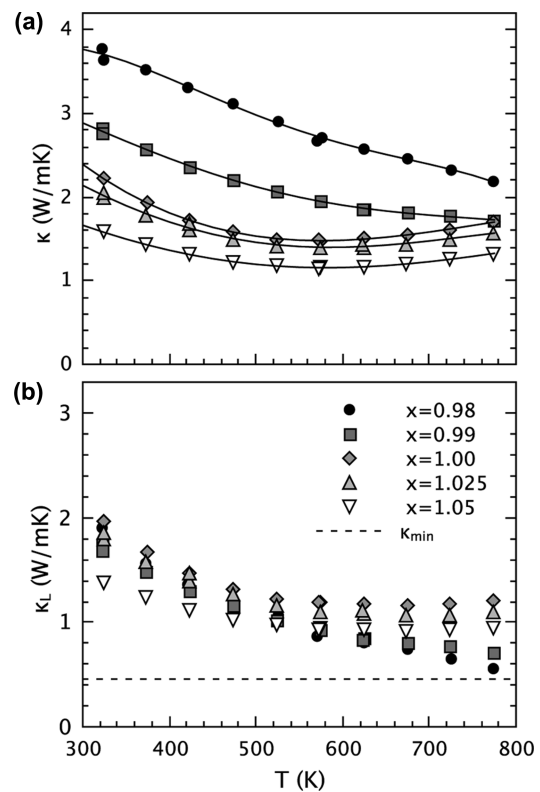**Figure 9.** (a) Total and (b) lattice thermal conductivity of $Yb_xZn_2Sb_2$ samples. The Yb content has little effect on the magnitude of κ_L.

function of temperature. The total thermal conductivity, calculated using the Dulong Petit heat capacity and experimental density, decreases with increasing x, due to the decreasing electronic contribution, κ_e. κ_e was estimated using the Wiedemann–Franz relationship $(\kappa_e = LT/\rho)$, where L was approximated using a single parabolic band model. Subtracting κ_e from κ yields the lattice and bipolar contributions (Figure 9b), the latter of which is apparent in samples with $x = 1.00–1.05$ above 600 K. The lattice contribution decreases slightly with increasing Yb content, contrary to what one might expect if Yb vacancies act as phonon scattering centers. One potential explanation for this trend is the expansion of the lattice (Figure 3b), and the corresponding increase in the anisotropic thermal parameters with increasing Yb content.

Previous reports of the thermoelectric properties of AM_2Sb_2 phases have focused on alloying with isovalent elements on the A and M sites to induce point defect scattering and reduce κ_L.[6,18–21,23,24] This strategy results in significant reductions to κ_L at room temperature, but much less reduction at higher temperatures where Umklapp phonon–phonon scattering already limits κ_L.[4] Indeed, at 773 K, Umklapp scattering reduces κ_L nearly to the minimum predicted lattice thermal conductivity, κ_{min}, which is shown as the dashed curve in Figure 9b. Here, κ_{min} was calculated using $\kappa_{min} = \frac{1}{2}(\pi/6)^{1/3}k_B V^{-2/3}(2\nu_T + \nu_L)$,[5,46] where the longitudinal and transverse sound velocities are given by $\nu_L = 3400$ m/s and $\nu_T = 1850$ m/s, respectively.

Figure of Merit. In all previous studies, carrier concentration control in AM_2Sb_2 phases has been accomplished using isoelectronic substitutions, thus inadvertently exploiting the low defect formation energies in this system. For example, substitutions of either Cd^{2+} or Mn^{2+} on the Zn^{2+} site or Ca^{2+} on the Yb^{2+} site have been shown to reduce the hole concentrations in $YbZn_2Sb_2$, leading to improved zT values.[18,19,22] The disadvantage of such strategies is that control of the Fermi level cannot be decoupled from solid solution effects such as point defect scattering of phonons and charge carriers, and potentially significant changes to the band structure.[47–49] In the present study, the carrier concentration is controlled independently, allowing for the first time the optimization of unalloyed $Yb_xZn_2Sb_2$ within a simple single parabolic band model, as shown in Figure 10. The dashed curve
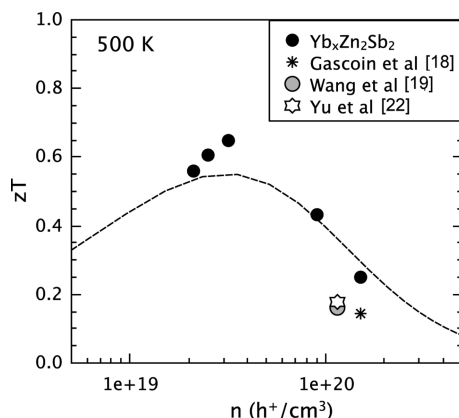

Figure 10. Figure of merit of $Yb_xZn_2Sb_2$ samples is optimized within a single parabolic band model (dotted curve) when $n_H = 3 \times 10^{19}$ h$^+$/cm^3. In previously reported, nominally stoichiometric $YbZn_2Sb_2$ samples, n_H was significantly higher than optimal.[18,19,22]

was generated using the following parameters at 500 K: $m^* = 0.9\ m_e$, $\mu_o = 130$ cm^2/(V s), and $\kappa_L = 0.9$ W/mK. The predicted optimal n_H is 3×10^{19} h$^+$/cm^3 and agrees well with experimental zT values.

These results raise the question of why previously reported $YbZn_2Sb_2$ samples exhibited larger carrier concentrations than the nominally stoichiometric sample $(x = 1.00)$ in the current study. One potential explanation might be differences in the synthetic process leading to an inadvertent Yb deficiency, and thus to the higher observed n_H. In all previous reports, samples were first heated to above 1000 °C for between 30 and 72 h, before being slowly cooled, and then consolidated at 450 °C.[18,19,22] The initial high-temperature step may have led to Yb vaporization or reaction with the container. Regardless of the cause, the presence of ZnSb as a secondary phase in all previous studies confirms that they were indeed Yb-deficient. In contrast, a low-temperature, solid-state synthesis route was employed in the current study and ZnSb was not observed as a secondary phase in any samples.

The figure of merit, shown in Figure 11 as a function of temperature, was calculated using the polynomial fits shown in
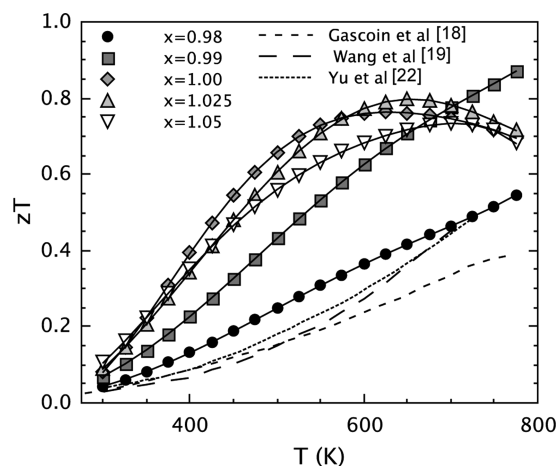

Figure 11. Peak and average zT in $Yb_xZn_2Sb_2$ are significantly improved relative to previous reports[18,19,22] due to the reduced carrier concentrations.

Figures 7a,d and 9a. At 800 K, the sample with $x = 0.99$ has a peak zT of 0.85. In the samples with higher Yb content, the average zT is greatly improved, but it falls off above 650 K due to minority carrier effects, leading to a lower maximum zT. Previously reported peak zT values in unalloyed $YbZn_2Sb_2$ range from 0.4[18] to 0.55.[19] Thus, by optimizing the samples within a single band model, both the average and the peak zT of $Yb_xZn_2Sb_2$ can be significantly enhanced. We expect that this method could be applied successfully to other compounds with the $CaAl_2Si_2$ structure type, including AZn_2Sb_2, AMg_2Bi_2, and AMg_2Sb_2 compounds (A = Sr, Ca, Yb, Eu), all of which exhibit degenerate semiconducting behavior indicative of cation vacancies.[25,30,31]

■ CONCLUSION

Our experimental investigation of $Yb_xZn_2Sb_2$ (x = 0.98, 0.99, 1.00, 1.025, 1.05) confirms previous computational results indicating that nonstoichiometry in this phase is responsible for the large experimental carrier concentrations. In Yb-deficient samples ($x < 1.00$), the lattice parameters were found to

decrease linearly and the bond angles in the distorted Zn—Sb tetrahedra were found to approach the ideal tetrahedral geometry with decreasing Yb. By varying x, we found that the p-type carrier concentration can be controlled within a relatively wide single phase region. In the most Yb-deficient sample, the maximum carrier concentration obtained agrees well with the calculated Yb-deficient stability limit (i.e., solvus line). By using the nominal Yb content, x, to tune the carrier concentration, significant improvements in the average and peak zT of $YbZn_2Sb_2$ were achieved. These results may provide a new route to understanding and controlling the electronic properties in many other compounds with the $CaAl_2Si_2$ structure type, potentially leading to further increases in thermoelectric performance.

■ ASSOCIATED CONTENT

Ⓢ Supporting Information

Figures S 1— S 5 show complete synchrotron X-ray diffraction data for all compositions including profile fits, profile differences, and TICS from the corresponding Rietveld refinements. This material is available free of charge via the Internet at http://pubs.acs.org.

■ AUTHOR INFORMATION

Corresponding Authors

*E-mail: jsnyder@caltech.edu (J.S.).
*E-mail: sabah.k.bux@jpl.nasa.gov (S.B.).

Notes

The authors declare no competing financial interest.

■ ACKNOWLEDGMENTS

■ REFERENCES

(1) Snyder, G. J.; Toberer, E. S. *Nat. Mater.* **2008**, *7*, 105−114.

(2) Kauzlarich, S. M., Ed. *Chemistry, Structure, and Bonding of Zintl Phases and Ions*; Wiley-VCH: New York, 1996.

(3) Mills, M.; Lam, R.; Ferguson, M. J.; Deakin, L.; Mar, A. *Coord. Chem. Rev.* **2002**, *233−234*, 207−222.

(4) Toberer, E. S.; May, A. F.; Snyder, G. J. *Chem. Mater.* **2010**, *22*, 624−634.

(5) Toberer, E. S.; Zevalkink, A.; Snyder, G. J. *J. Mater. Chem.* **2011**, *21*, 15843.

(6) Guo, K.; Cao, Q.-G.; Feng, X.-J.; Tang, M.-B.; Chen, H.-H.; Guo, X.; Chen, L.; Grin, Y.; Zhao, J.-T. *Eu. J. Inorg. Chem.* **2011**, *2011*, 4043−4048.

(7) Toberer, E. S.; Cox, C. A.; Brown, S. R.; Ikeda, T.; May, A. F.; Kauzlarich, S. M.; Snyder, G. J. *Adv. Funct. Mater.* **2008**, *18*, 2795−2800.

(8) Zevalkink, A.; Zeier, W. G.; Pomrehn, G.; Schechtel, E.; Tremel, W.; Snyder, G. J. *Energy Environ. Sci.* **2012**, *5*, 9121.

(9) Holm, A. P.; Park, S.-M.; Condron, C. L.; Kim, H.; Klavins, P.; Grandjean, F.; Hermann, R. P.; Long, G.-J.; Kanatzidis, M. G.; Kauzlarich, S. M. *Inorg. Chem.* **2003**, *42*, 4660−4667.

(10) Wang, J.; Xia, S. Q.; Tao, X. T. *Chem.—Asian J.* **2013**, *8*, 251−7.

(11) Wang, J.; Yang, M.; Pan, M. Y.; Xia, S. Q.; Tao, X. T.; He, H.; Darone, G.; Bobev, S. *Inorg. Chem.* **2011**, *50*, 8020−8027.

(12) Park, S.-M.; Kim, S.-J.; Kanatzidis, M. G. *Inorg. Chem.* **2001**, *40*, 3781−3785.

(13) Kim, S.-J.; Hu, S.; Uher, C.; Kanatzidis, M. G. *Chem. Mater.* **1999**, *11*, 3154−3159.

(14) Park, S. M.; Kim, S.-J.; Kanatzidis, M. G. *J. Solid State Chem.* **2004**, *177*, 2867−2874.

(15) Lam, R.; Mar, A. *Inorg. Chem.* **1996**, *35*, 6959−6963.

(16) Pomrehn, G.; Zevalkink, A.; Zeier, W. G.; van de Walle, A.; Snyder, G. J. *Angew. Chem., Int. Ed.* **2014**, *53*, 3422−3426.

(17) Burdett, J. K.; Miller, G. J. *Chem. Mater.* **1990**, *2*, 12−26.

(18) Gascoin, F.; Ottensmann, S.; Stark, D.; Haile, M. S.; Snyder, G. *Adv. Funct. Mater.* **2005**, *15*, 1860−1864.

(19) Wang, X.-J.; Tang, M.-B.; Chen, H.-H.; Yang, X.-X.; Zhao, J.-T.; Burkhardt, U.; Grin, Y. *Appl. Phys. Lett.* **2009**, *94*, 092106.

(20) Zhang, H.; Baitinger, M.; Tang, M. B.; Man, Z. Y.; Chen, H. H.; Yang, X. X.; Liu, Y.; Chen, L.; Grin, Y.; Zhao, J. T. *Dalton Trans.* **2010**, *39*, 1101−1104.

(21) Cao, Q.-G.; Zhang, H.; Tang, M.-B.; Chen, H.-H.; Yang, X.-X.; Grin, Y.; Zhao, J.-T. *J. Appl. Phys.* **2010**, *107*, 053714.

(22) Yu, C.; Zhu, T. J.; Zhang, S. N.; Zhao, X. B.; He, J.; Su, Z.; Tritt, T. M. *J. Appl. Phys.* **2008**, *104*, 013705.

(23) Zhang, H.; Zhao, J. T.; Grin, Y.; Wang, X. J.; Tang, M. B.; Man, Z. Y.; Chen, H. H.; Yang, X. X. *J. Chem. Phys.* **2008**, *129*, 164713.

(24) Zhang, H.; Fang, L.; Tang, M.-B.; Chen, H.-H.; Yang, X.-X.; Guo, X.; Zhao, J.-T.; Grin, Y. *Intermetallics* **2010**, *18*, 193−198.

(25) Toberer, E. S.; May, A. F.; Melot, B. C.; Flage-Larsen, E.; Snyder, G. J. *Dalton Trans.* **2010**, *39*, 1046−54.

(26) May, A. F.; McGuire, M. A.; Ma, J.; Delaire, O.; Huq, A.; Custelcean, R. *J. Appl. Phys.* **2012**, *111*, 033708.

(27) Flage-Larsen, E.; Diplas, S.; Prytz, Ø.; Toberer, E. S.; May, A. F. *Phys. Rev. B* **2010**, *81*, 205204.

(28) Zevalkink, A.; Pomrehn, G. S.; Johnson, S.; Swallow, J.; Gibbs, Z. M.; Snyder, G. J. *Chem. Mater.* **2012**, *24*, 2091−2098.

(29) Zevalkink, A.; Toberer, E. S.; Zeier, W. G.; Flage-Larsen, E.; Snyder, G. J. *Energy Environ. Sci.* **2011**, *4*, 510.

(30) May, A. F.; McGuire, M. A.; Singh, D. J.; Custelcean, R.; Jellison, J. G. E. *Inorg. Chem.* **2011**, *50*, 11127−33.

(31) May, A. F.; McGuire, M. A.; Singh, D. J.; Ma, J.; Delaire, O.; Huq, A.; Cai, W.; Wang, H. *Phys. Rev. B* **2012**, *85*, 035202.

(32) Ertekin, E.; Srinivasan, V.; Ravichandran, J.; Rossen, P. B.; Siemons, W.; Majumdar, A.; Ramesh, R.; Grossman, J. C. *Phys. Rev. B* **2012**, *85*, 195460.

(33) May, A. F.; Toberer, E. S.; Saramat, A.; Snyder, G. J. *Phys. Rev. B* **2009**, *80*, 125205.

(34) Parada, N. J.; Pratt, G. W. J., Jr. *Phys. Rev. Lett.* **1969**, *22*, 180.

(35) Bjerg, L.; Madsen, G. K. H.; Iversen, B. B. *Chem. Mater.* **2012**, *24*, 2111−2116.

(36) Larson, A. C.; Dreele, R. B. V. *General Structure Analysis System (GSAS)*; Los Alamos National Laboratory Report LAUR 86-748; The Regents of the University of California: Oakland, CA, 2004; pp 86−748.

(37) Wood, C.; Zoltan, D.; Stapfer, G. *Rev. Sci. Instrum.* **1985**, *56*, 719.

(38) Borup, K. A.; Toberer, E. S.; Zoltan, L.; Nakatsukasa, G.; Errico, M.; Fleurial, J.; Iverson, B.; Snyder, G. J. *Rev. Sci. Instrum.* **2012**, *83*, 123902.

(39) Ohno, S.; Zevalkink, A.; Takagiwa, Y.; Bux, S. K.; Snyder, G. J. *J. Mater. Chem. A* **2014**, *2*, 7478−7483.

(40) Schellenberg, I.; Eul, M.; Hermes, W.; Pöttgen, R. *Z. Anorg. Allg. Chem.* **2010**, *636*, 85−93.

(41) Mewis, A. *Z. Naturforsch., B* **1978**, *33*, 382.

(42) Pomrehn, G.; Toberer, S.; Snyder, G. J.; van de Walle, A. *Phys. Rev. B* **2011**, *83*, 094106.

(43) Alemany, P.; Llunell, M.; Canadell, E. *J. Comput. Chem.* **2008**, *29*, 2144−2153.

5716

dx.doi.org/10.1021/cm502588r | *Chem. Mater.* 2014, 26, 5710−5717

(44) Kranenberg, C.; Johrendt, D.; Mewis, A. *Z. Anorg. Allg. Chem.* **1999**, *625*, 1787−1793.

(45) Ravich, Yu. I.; Efimova, B. A.; Smirnov, I. A. In *Semiconducting lead chalcogenides*; Stilbans, L. S., Ed.; Plenum Press: New York, 1970.

(46) Cahill, D.; Watson, S.; Pohl, R. *Phys. Rev. B* **1992**, *46*, 6131−6140.

(47) Abeles, B.; Beers, D. S.; Cody, G. D.; Dismukes, J. P. *Phys. Rev.* **1962**, *125*, 44−46.

(48) Wang, H.; Pei, Y. Z.; LaLonde, A. D.; Snyder, G. J. *Adv. Funct. Mater.* **2013**, *23*, 1586−1596.

(49) Pei, Y.; Shi, X.; LaLonde, A.; Wang, H.; Chen, L.; Snyder, G. J. *Nature* **2011**, *473*, 66−9.